1

Near-Field Hierarchical Beam Training for Reconfigurable Holographic Surfaces

Yinuo Dong, Qingchao Li, (Member, IEEE), Soon Xin Ng, (Senior Member, IEEE), Mohammed El-Hajjar, (Senior Member, IEEE)

Abstract—Reconfigurable holographic surfaces (RHS) are expected to play a key role in future mobile networks. However, the substantial increase in antenna aperture and operating frequency brings new challenges for near-field communication. We propose a near-field multi-user 3D hierarchical beam training scheme tailored for RHS-based multi-input multi-output (MIMO) systems, supporting both near-field and far-field user deployment, while considering hardware constraints. Since the hierarchical beam training scheme involves activating varying numbers of transmitting elements at each search layer, and RHS elements are densely packed, significant mutual coupling effects may arise. To mitigate this, we propose two element activation strategies: centered activation and sparse activation based on different RHS element positioning patterns within the hierarchical beam training framework. Furthermore, we design a practical beam training approach tailored to a hybrid digital-holographic architecture, optimized through an alternating algorithm that accounts for both binary and coupled amplitude-phase hardware constraints on RHS meta-elements. Simulation results demonstrate strong robustness under various hardware and channel state information (CSI) imperfections, achieving performance close to that of fully digital systems. Finally, we further analyse the asymptotic orthogonality of near-field beam focusing vectors under different RHS surface geometries. The results show that rectangular surfaces offer superior beam orthogonality for beams steered in the same direction but located at different distances.

Index Terms—Near-field, Hierarchical Beam Training, Beam Training, Reconfigurable Holographic Surfaces.

I. INTRODUCTION

Driven by the rapid proliferation of smart devices and advanced applications, future 6G networks are expected to achieve peak data rates of up to 100 Gb/s [1]. To meet this demand, extremely large-scale antenna arrays (XL-arrays) have emerged as a promising solution. However, although these high-rate schemes offer greater communication quality, they also impose higher demands on power consumption and increased hardware complexity, which have emerged as major technical bottlenecks in highly integrated antennas and massive multi-input multi-output (MIMO) systems [2].

To address these challenges, reconfigurable holographic surfaces (RHS) with its continuous aperture and controllable

The authors are with the School of Electronics and Computer Science, University of Southampton, Southampton SO17 1BJ, United Kingdom. (e-mail: yd4u21@soton.ac.uk; Qingchao.Li@soton.ac.uk; sxn@ecs.soton.ac.uk; meh@ecs.soton.ac.uk).

Mohammed El-Hajjar would like to acknowledge the support of the Future Telecoms Research Hub, Platform for Driving Ultimate Connectivity (TITAN), sponsored by the Department of Science Innovation and Technology (DSIT) and the Engineering and Physical Sciences Research Council (EPSRC) under Grants EP/X04047X/1, EP/Y037243/1 and EP/X04047X/2.

phase and amplitude radiation elements offers a practical solution to achieve low-cost, high-directional gain [3]. Specifically, RHS consists of a feed source and radiation elements based on metamaterials, where the feed source connects the radio frequency (RF) chain to the RHS circuitry. These architectures convert input signals into electromagnetic waves and achieve holographic beamforming by electronically controlling the coefficients of the radiation elements [4]. Compared to traditional phase shifters, RHS has lower power consumption, scalability, and suitability for large-scale integration and packaging [5].

The RHS enables flexible beam steering and control by dynamically adjusting the electromagnetic response on its surface, offering a more efficient and adaptable approach to wireless communication [6]. The RHS provides significant advantages in terms of flexible beamforming and directional control, while also reducing the complexity of the system hardware and power consumption.

To effectively harness these advantages, various hybrid beamforming strategies tailored for RHS architecture have been investigated. However, the extremely large scale MIMO and RHS typically employs hundreds or even thousands of elements, that leads to a sharp increase in the aperture, which can result in a fundamental change of the electromagnetic (EM) characteristics [7] and the corresponding near-field region expands accordingly. Moreover, the deployment of RHS is expected to significantly enhance spatial resolution, thus achieving substantial spatial multiplexing gains. To realize these gains, the RHS must generate highly directional beams with substantial array gain through beamforming. In [8] [9], Deng et al. proposed an RHS-based hybrid beamforming scheme, where the digital beamformer and the holographic beamformer are performed in the BS and the RHS, respectively. Specifically, the digital beamformer relies on the state-of-the-art zero-forcing (ZF) precoding method, while the holographic beamforming is performed by configuring the amplitude-controlled RHS radiation elements. In [10] [11], Li et al. proposed the hybrid beamforming design of the switch-controlled RHS architecture, and proposed an energy efficiency maximization problem for switch-controlled RHSenabled wireless communication systems operating in the face of realistic hardware impairments of the transceiver. Additionally, researches on beamforming design of large-scale reconfigurable surfaces in near-field scenarios, such as the study by Zhang et al. [12], explored the potential of beam focusing using fully-digital, phase shifter-based hybrid, and dynamic metasurface antenna architectures. The study demonstrates the feasibility of these architectures in near-field operations.

TABLE I
NOVELTY COMPARISON WITH THE LITERATURE

	Our paper	[8]	[9]	[10]	[13]	[14]	[15]	[16]	[17]	[18]	[19]	[20]
Multi-user	√		√				√					√
Near-field and Far-field	√					✓		√	√			√
Hardware Constrains	√		✓	✓	✓	√						
Hybrid Structure	√	√	√	√	√					√		
Hierarchical Beam Training	√				√	√			√		√	√
Beam Correlation Analysis	√						√					
RHS Mutual Coupling	√											

However, to circumvent the need for accurate channel state information (CSI), beamforming can be implemented through codebook-based design and beam training. Specifically, the optimal codeword is selected from a predefined codebook to best match the user's channel prior to beamforming. In [14], [16]-[19], [21]-[26] the near-field beam training based on large-scale antenna array was analyzed. In [16] Wu et al. proposed a scheme to jointly estimate the user angle and range with the DFT codebook. In [17] and [18], the authors proposed a two-stage beam training method and a two-stage hierarchical beam training method. These methods decompose the two-dimensional search into two sequential phases, reducing the near-field beam-training overhead. In the first phase, candidate angles are determined using a new approach based on the conventional far-field codebook and angle-domain beam sweeping. In the second phase, a customized polar-domain codebook is used to find the best effective distance for the user based on the shortlisted angles. In [19], another near-field hierarchical codebook was proposed, along with a steering beam gain approximation method. The lower-layer codebook is designed to provide coverage for the Fresnel region. For the upper-layer codebook, beam rotation and beam relocation methods are introduced to position an arbitrary beam pattern at a target location. In [21], Wu et al. design a concentric-ring codebook to achieve efficient codebook-based beamforming in the near-field region for a uniform circular array (UCA) to provide uniform and enlarged near-field regions at all angles. Then, in [22] a polar-domain representation that simultaneously accounts for both the angular and distance information in near-field domain was proposed, which proves that the near-field beam training requires a beam search over both the angular and distance domains due to the spherical wavefront propagation model. In [23], Zhou et al. proposed a sparse discrete Fourier transform (DFT) codebook to address the unaffordable beam training overheading both angular domain and distance domain.

Above all, the aforementioned beam training schemes and codebook designs are all based on extremely large-scale antenna arrays (ELAA) and extremely large-scale large-scale MIMO (XL-MIMO), which are typically designed based on angular domain alignment and distance-domain focusing within the near-field region. Although RHS and planar ELAAs share similar spatial configurations—both operating in three-dimensional space—the RHS architecture imposes fundamentally different hardware constraints, including coupled amplitude-phase responses, mutual coupling, and limited feed structures [27]. These differences necessitate a distinct beam

training strategy as proposed in this work, which explicitly incorporates holographic-specific impairments into both the hierarchical codebook design and the orthogonality analysis. For example, [20] proposed a low-complexity multi-user beamforming method based on RHS for both near- and farfield scenarios, while it does not take into account specific hardware features of the RHS.

On the other hand, the physical deployment of RHSs has a significant impact on system-level beam training performance. Recent results in [28] emphasized that practical RHS deployments must consider the tradeoffs between hardware limitations, propagation geometry, and user field-of-view coverage. Furthermore, the impact of physical deployment and nearfield electromagnetic nonstationarities has been highlighted in [27], which shows that spatially varying visibility regions induce location, dependent array gains and phase distortions, posing significant challenges to conventional beamforming and codebook alignment.

Complementary to this, recent works have leveraged highdimensional RIS responses to enhance localization accuracy via learning-based frameworks. For example, [29] employed convolutional neural networks (CNN) and transfer learning to extract spatial features from RIS reflections, enabling accurate localization under limited training data. In parallel, [30] investigated the impact of hardware faults in RIS elements and introduces a fault-aware learning framework that maintains localization robustness despite physical impairments.

Due to the unique architecture of RHS, where elements are densely packed and their behavior is influenced by metamaterial properties and fabrication variabilities [31], the commonly assumed independent control of amplitude and phase is impractical in real implementations. Therefore, we aim to design a practical low-complexity RHS beam training scheme considering discrete or coupled amplitude-phase in holographic processes, as well as mutual coupling effects between closely spaced elements in near-field scenarios. To capture these effects, we develop a hardware-aware beam training scheme under a hybrid digital-holographic architecture, and propose two distinct element activation schemes to assess and mitigate mutual coupling. These considerations are essential to bridge the gap between theoretical analysis and deployable RHS-based communication systems.

Moreover, while the spatial domain is coupled with a large number of elements present in the RHS, exhaustive search methods are impractical. Consequently, it is imperative to develop a cost-effective hierarchical search scheme. Although [20] proposed a low-complexity hierarchical beam training approach, it adopts a two-stage strategy in which distance is searched separately following a coarse angular estimation. This design assumes that the angular estimate is sufficiently accurate to allow for a decoupled one-dimensional distance search, an assumption that becomes questionable in near-field scenarios. For instance, using a 6-layer binary hierarchical angular search in the first stage yields an angular resolution of approximately $180^{\circ}/2^{6} = 2.8^{\circ}$, which introduces a nonnegligible estimation error. According to the spherical wavefront model [32], the distance parameter r affects the phase response as $e^{(\cdot)/r}$, and for r > 1 m, variations in r contribute minimally to the overall phase. Furthermore, although the spherical wavefront can naturally span a certain angular range, this property becomes less reliable when accounting for hardware-induced offsets and the extremely narrow beams resulting from ultra-large-scale arrays, leading to increased estimation errors. As a result, even moderate angular errors can severely degrade the effectiveness of subsequent distance refinement, often preventing the system from achieving the desired beamwidth resolution. Motivated by this, we advocate for a joint angle-distance sampling strategy in the top hierarchical layers to enhance robustness and accuracy, which is particularly practical given the beamwidth limitations imposed by RHS constraints.

While the aforementioned studies primarily focus on beamforming and training under static RHS or RIS configurations, recent advancements in reconfigurable antenna technologies have introduced new opportunities for spatial diversity and adaptability. As comprehensively reviewed in [33], fluid antenna system (FAS) architectures exhibit significant potential in supporting critical services such as ultra-reliable low-latency communications (URLLC), intelligent sensing, and physicallayer security, owing to their inherent electromagnetic reconfigurability and spatial agility. Building upon this foundation, [34] proposed a deep reinforcement learning (DRL)-based intelligent antenna positioning algorithm for FAS-assisted ISAC systems, enabling environment-aware beam placement under mobility and latency constraints. In a complementary study, [35] investigated the security implications of FAS-RIS hybrid systems by introducing a block-correlation model, revealing how spatial correlation among elements affects the average secrecy capacity and outage probability.

The contributions in this paper can be summarized as follows:

- We propose a practical multi-user hierarchical beam training scheme based on holographic principles, which is flexible and adaptable to both near- and far-field scenarios. Compared to existing ELAA and RHS based beam training methods, the proposed scheme is particularly practical when accounting for discrete binary or coupled amplitude-phase characteristics inherent in holographic implementations, rather than assuming idealized conditions
- Additionally, considering the large number of elements densely arranged on the RHS result in significant mutual coupling, this effect must be carefully addressed [36].
 To account for this, we propose two different element activation schemes within the hierarchical beam training

- framework. In the first scheme, the elements are activated in the central region of the RHS, while in the second, they are activated sparsely. We then compare the mutual coupling effects between these two schemes in the context of hierarchical beam training design.
- Given that a fully digital architecture with high energy consumption is impractical in an RHS system, we design a practical beam training scheme tailored to a hybrid digital-holographic architecture. Hence, we propose an alternating optimization algorithm to derive the practical codeword. Specifically, considering the metamaterial elements on the RHS surface, which can be modeled as resonant electrical circuits, their frequency responses are typically characterized by amplitude-only, binary amplitude, or Lorentzian phase constrain [13].
- Moreover, we investigated the asymptotic orthogonality
 of near-field beam focusing vectors generated by different
 holographic surface shapes. The theory and simulation
 results both indicate that a rectangular surface achieves
 better beam orthogonality for beams oriented in the same
 direction but at different distances in near-field scenarios.
- By simulations, we prove that the proposed alternating optimization algorithm efficiently converges in fewer than eight iterations under hardware-constrained RHS-aided hybrid beamforming, demonstrating fast convergence suitable for practical implementations. We also simulated the results with different numbers of RF chains under multi-user scenarios. The simulation results demonstrate that the beam training optimization algorithm performs effectively and approaches full digital performance, even under a hardware-constrained multi-user hybrid architecture.

In order to highlight the contributions of this paper relative to other existing works, Table I provides a comparative analysis of key features in various studies.

The rest of this paper is organized as follows: we firstly introduce the system model and beam training scheme in Section II and Section III. Then, we analyze the asymptotic orthogonality of near-field beam focusing vectors for RHSs of different sizes and the training overhead for the proposed schemes in Section IV. Finally, we present the simulation results of the different proposed schemes in Section V.

II. SYSTEM MODEL

In this section, we briefly highlight the system model of the considered RHS-aided hybrid beamforming architecture and codebook design, while communicating in near field scenarios.

A. Signal Model

We consider an RHS-aided near-field scenario in which the base station (BS) employs a $N=N_x\times N_y$ uniform planar array holographic element surface with M RF chains to serve K single antenna users. Consider an RHS surface located at the origin, with N_x elements along the x-axis and N_y elements along the y-axis. Let $\mathbf{H}=[\mathbf{h}_1,\ldots,\mathbf{h}_K]^{\mathrm{T}}\in\mathbb{C}^{N\times K}$ denote the channel matrix between the transmission side and the users.

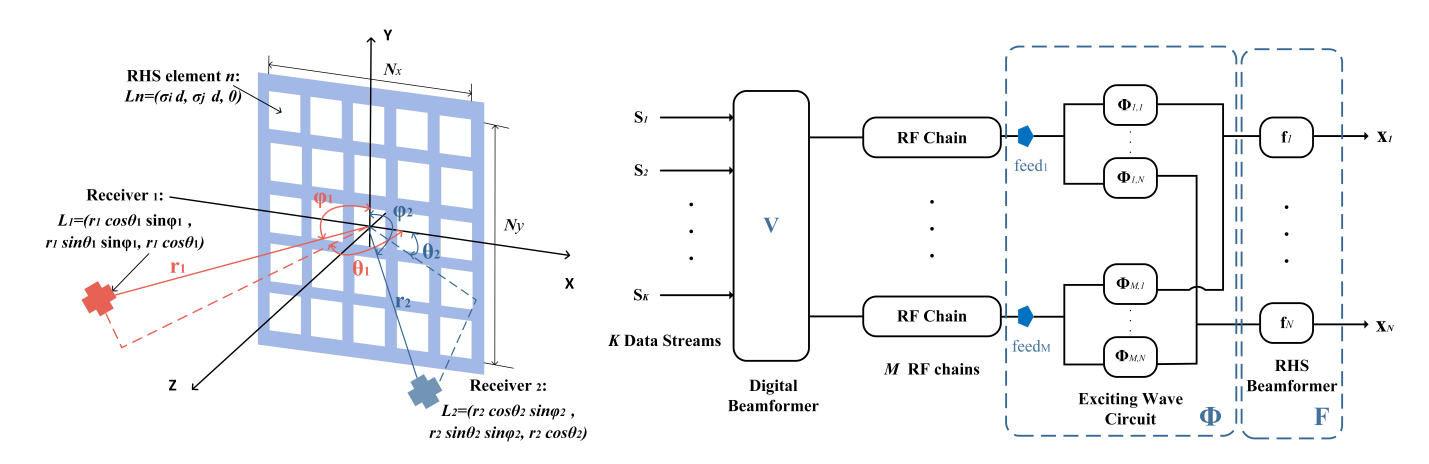


Fig. 1. System model and hybrid architecture of reconfigurable holographic surface.

The general multi-path channel from the RHS to the user can be modeled as

$$\mathbf{h}_{k} = \sqrt{N}\bar{h}_{k}\mathbf{b}(\theta_{k}, \phi_{k}, r_{k}) + \sum_{i}^{I} \sqrt{\frac{N}{I}}\tilde{h}_{k,i}\mathbf{b}(\bar{\theta}_{k}, \bar{\phi}_{k}, \bar{r}_{k}), \quad (1)$$

where the complex channel gain are the line-of-sight (LoS) channel $\bar{h}_k = \sqrt{\frac{\kappa}{1+\kappa}} \frac{\sqrt{\rho_0}}{r_k} e^{-j\frac{2\pi}{\lambda_c} r_k}$ and the non-line-of-sight (NLoS) channel $\tilde{h}_k = \sqrt{\frac{1}{1+\kappa}} \frac{\sqrt{\rho_0}}{r_k} e^{-j\frac{2\pi}{\lambda_c} r_k}$, while the κ represents the Rician factor and ρ_0 denotes the channel gain at the reference distance of 1 m and I denote the number of NLoS paths, respectively. The θ_k and ϕ_k denote the azimuth and elevation angles of user k in the spherical coordinate system, respectively, and r_k represents the radial distance from user k to the center of the RHS aperture.

In this paper, we focus on RHS assisted near-field communication scenarios within high-frequency bands. In these environments, the power of NLoS channel paths is significantly attenuated due to severe path loss and shadowing effects [23] [37] [15]. As a result, our analysis is restricted to the main path, that is, the LoS channels, where the BS-user channel can be closely approximated by the LoS path alone, using the uniform spherical wave (USW) model [38]. The near-field LoS channel from the BS to the user can be characterized as

$$\mathbf{h}_k = \sqrt{N}\bar{h}_k \mathbf{b}_k (\theta_k, \phi_k, r_k), \tag{2}$$

where θ_k , ϕ_k , and r_k represent the azimuth and elevation angles, and the distance from the transmitter to user k and the center of the RHS surface, respectively. Moreover, $\mathbf{b}_k(\cdot)$ is the steering vector of the kth user, which derived based on the spherical wave model, where it samples both the angles and the distance as follows [38]

$$\mathbf{b}(\theta, \phi, r) = \frac{1}{\sqrt{N}} \left[e^{-j\frac{2\pi}{\lambda_c}(r^{(1,1)} - r)}, \dots, e^{-j\frac{2\pi}{\lambda_c}(r^{(1,N_y)} - r)}, \dots, e^{-j\frac{2\pi}{\lambda_c}(r^{(N_x,1)} - r)}, \dots, e^{-j\frac{2\pi}{\lambda_c}(r^{(N_x,N_y)} - r)} \right]^T, \quad (3)$$

where $r^{(i,j)}$ indicates the distance between the (i,j)th element of the RHS and the user.

The location of the (n_x,n_y) th element can be expressed as $U_{\rm element}^{(n_x,n_y)}=[\delta_{n_x}d,\delta_{n_y}d,0]$, where $\delta_{n_x}=\frac{2n_x-N_x+1}{2}$ and

 $\delta_{n_y}=rac{2n_y-N_y+1}{2}, ext{ for } n_x=1,\ldots,N_x ext{ and } n_y=1,\ldots,N_y.$ While the location of the ku user can be represented as $L_k=[r_k\cos\theta_k\sin\phi_k-\delta_{n_x},r_k\cos\theta_k\sin\phi_k-\delta_{n_x},r_k\cos\phi_k]$ The distance from the kth user to the (n_x,n_y) th element of the surface is then given by

$$r_k^{(n_x,n_y)} = \sqrt{(L_k^{(x)} - \delta_{n_x} d)^2 + (L_k^{(y)} - \delta_{n_y} d)^2 + (L_k^{(z)})^2}.$$
 (4)

Unlike Dynamic Metasurface Antennas (DMA) and Holographic MIMO (HMIMO) architectures [39], where each feed point connects to a row of metamaterial antennas in a subconnected manner without requiring additional phase shifters, the considered RHS adopts a fully connected architecture with calibration phase shifters. This design provides finer-grained beam control and higher beamforming flexibility, at the expense of increased hardware complexity [11]. Compared to DMA and HMIMO, the RHS enables continuous holographic beamforming with improved near-field focusing capability.

We assume in this paper that the user is located in the Fresnel region and not exceed Rayleigh distance, i.e. $r > r_{\min} = \max\left\{\frac{1}{2}\sqrt{\frac{D^3}{\lambda_c}}, 1.2D\right\}$ and $r < r_{\max} = \frac{D^2}{\lambda_c}$, where D and λ_c denote the aperture size of the array and the carrier wavelength, respectively. In this region, the amplitude variations between the antennas are considered negligible [38] [32]. It is also worth noting that when the r is sufficiently large, $r_k^{(n_x,n_y)} \approx r_k - (\delta_{n_x}\cos\theta_k\sin\phi_k - \delta_{n_y}\sin\theta_k\sin\phi_k)d$, where $\delta_{n_x} = \frac{2n_x - N_x - 1}{2}$ and $\delta_{n_y} = \frac{2n_y - N_y - 1}{2}$. Then, in this case $\mathbf{b}(\theta,\phi,r)$ is equivalent to the conventional far-field steering vector

$$\mathbf{a}(\theta,\phi) = \frac{1}{\sqrt{N}} [1, \cdots, e^{j\pi(n_x \sin\phi \cos\theta + n_y \sin\phi \sin\theta)}, \cdots, e^{j\pi(N_x \sin\phi \cos\theta + N_y \sin\phi \sin\theta)}]^T.$$
 (5)

The received signal at the kth user is given by

$$y_k = \mathbf{h}_k^H \mathbf{w}_k x_k + \sum_{j \neq k} \mathbf{h}_k^H \mathbf{w}_j x_j + n_k,$$
 (6)

where the summation term $\sum_{j\neq k} \mathbf{h}_k^H \mathbf{w}_j x_j$ represents the multi-user interference, which can be effectively mitigated by employing precoding schemes [40]. The x_k denotes the symbol transmitted from the BS to the kth user, \mathbf{w}_k represents

the codeword of the kth user, and $n_k \sim \mathcal{CN}(0, \sigma^2)$ is the additive White Gaussian noise (AWGN) at the user with the power of σ^2 .

B. Problem formulation

In this paper, we aim to design an RHS-based multiuser near-field codebook, we formulate the design problem of a near-field codeword with optimal and hybrid RHS architecture, respectively.

From the above received signal model, it can be observed that the optimal codeword should align with the channel response, specifically $\mathbf{w}_k^* = \mathbf{b}_k(\theta_k, \phi_k, r_k)$. In practice, beam training is typically performed to establish a high-quality initial link prior to channel estimation and data transmission [17].

In the multi-user RHS-based system, to eliminate inter-user interference, singular value decomposition (SVD)¹ can be used to determine the optimal codeword design. Specifically, we denote the SVD of the baseband equivalent channel **H** as

$$\mathbf{H} = \mathbf{U} \mathbf{\Lambda} \mathbf{\Sigma}^H, \tag{7}$$

where $\Lambda = \{\lambda_1, \lambda_2, \dots, \lambda_K\}$ is a diagonal matrix with diagonal elements representing singular values in descending order, while $\mathbf{U} \in \mathbb{C}^{K \times K}$ and $\mathbf{\Sigma} \in \mathbb{C}^{N \times K}$ are complex-value unitary matrices. Since we focus on signal reception in this paper, the combining vector on the user's side is represented as a vector rather than a matrix. Consequently, the optimal codeword \mathbf{W}^* at the transmitter is designed as $\mathbf{W}^* = [\mathbf{w}_1^*, \dots, \mathbf{w}_K^*]^{\mathrm{T}} = \mathbf{\Sigma}$.

The ideal theoretical codeword **W*** can only be implemented using a fully digital architecture, where each antenna is equipped with a dedicated radio frequency (RF) chain to enable complete digital signal processing. However, in a holographic MIMO system, such a fully digital architecture results in prohibitively high energy consumption. Consequently, a hybrid architecture is often preferred to improve energy efficiency [10] [14]. Within this hybrid structure, it is essential to design practical codewords that account for hardware constraints, such as the frequency responses of RHS elements [13] and the limited number of RF chains.

Considering a hybrid RHS architecture shown in Fig. 1, the digital architecture with M RF chains and holographic architecture with N elements in an RHS, the digital beamforming vector for the kth user is $\mathbf{v}_k = [v_{1,k}, v_{2,k}, \dots, v_{M,k}] \in \mathbb{C}^{M \times 1}$ and the holographic beamforming matrix is $\mathbf{F} = \mathrm{Diag}\{\psi_1, \psi_2, \dots, \psi_N\} \in \mathbb{C}^{N \times N}$, where the ψ represents the phase adjusted on the elements, and include the effect of the hardware constraints of the RHS elements [13]. Details regarding to hardware constraints will be discussed later in section III.

To mitigate the impact of the location of the feed and RHS element, we employ an excitation wave circuit based on the discrete Fourier transform matrix (DFT) to define an excitation wave circuit matrix $\mathbf{\Phi} \in \mathbb{C}^{N \times M}$ [10]. In the excitation wave circuit between the mth feed and the nth

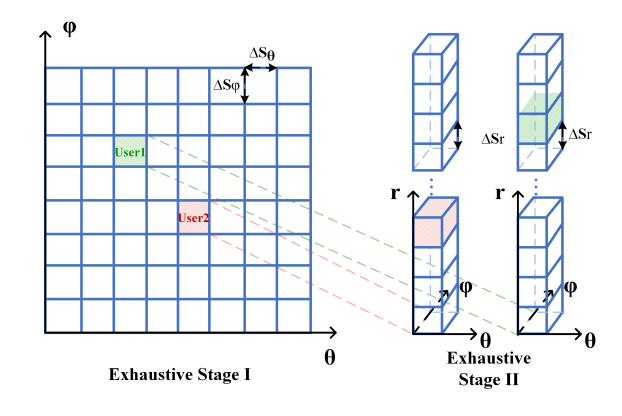


Fig. 2. Illustration of the two-stage exhaustive beam training scheme.

RHS element, a calibration phase shifter with a phase of $\Delta\phi_{n,m}=\frac{(n-1)(m-1)}{N}+k_0^{\rm T}\cdot r_n^m$ is applied to the reference wave, and the excitation wave is generated by

$$[\mathbf{\Phi}]_{n,m} = \frac{1}{\sqrt{N}} e^{j\left(-\mathbf{k}_0^{\mathrm{T}} \cdot \mathbf{r}_n^m + \Delta \phi_{n,m}\right)} = \frac{1}{\sqrt{N}} e^{j\frac{(n-1)(m-1)}{N}}, \quad (8)$$

where \mathbf{k}_0 is the propagation vector of the reference wave, and L_n^{element} is the position vector of the nth RHS element. The calibration phase shifters are only used for initial calibration and can be implemented digitally in practice, thus the additional hardware cost is negligible. They do not significantly increase the real-time complexity of the RHS system.

Consequently, the receive signal of the kth user in the RHS-aided MIMO system can be represented as

$$y_k = \mathbf{h}_k^{\mathrm{H}} \mathbf{F} \mathbf{\Phi} \mathbf{v}_k + n_k. \tag{9}$$

Having established the system model, the next section will introduce the design of an efficient beam training strategy tailored for RHS-aided MIMO systems.

III. BEAM TRAINING SCHEME

In this section, we present an exhaustive beam training scheme, followed by a proposed two-stage hierarchical method that is more adaptable to RHS structures under hardware constraints. In addition, we also introduce a practical beam training scheme.

This section proposes a novel hierarchical beam training strategy that differs from conventional near-field training by explicitly incorporating RHS-specific hardware constraints, including mutual coupling and practical element activation patterns. These aspects are not addressed in prior works on generic XL-MIMO beam training.

A. Two Stage Exhaustive Search Near-, Far-Field Beam Training

In near-field beam training, a beam search is required in both the angular and the distance domains [41]. For the scenario considered in this paper, a 3D search region encompasses the azimuth and elevation angles in the angular domain, as well as the distance domain.

Previous studies on near-field beam training schemes have made the following key observation: when far-field beams are

¹Although it is more practical to employ the ZF method for multi-user systems, the SVD method can help us unveil the performance limits of the RHS-based multi-user systems [10].

used for beam training, the true spatial direction of the nearfield user typically lies near the center of the dominant angular region, where beam power is sufficiently high [16]. Based on this observation, [17] proposed a two-stage beam training scheme. It is worth noting that this two-stage framework seamlessly generalizes to far-field scenarios, wherein the initial angular search aligns with classical beam training strategies.

In the exhaustive search beam training scheme, we also apply the two-stage scheme. In the first stage, we employ the far-field codebook to search on the angular domain, given by

$$\mathbf{w}_{(\mathcal{S}_1,\mathcal{S}_2)}^{\mathrm{FF}} = \{ \mathbf{a}(\theta_n^{(\mathcal{S}_1)}, \phi_n^{(\mathcal{S}_2)}) | \mathcal{S}_1 \in [0, \pi], \mathcal{S}_2 \in \left[-\frac{\pi}{2}, \frac{\pi}{2} \right] \}.$$

$$(10)$$

In far-field scenarios, the channel is primarily determined by the angular direction, whereas near-field beam training requires a joint search over both angular and distance domains. As illustrated in Fig. 2, Stage I performs an exhaustive search to identify the optimal angular direction. Based on the estimated angle from Stage I, Stage II refines the process by exhaustively searching the distance domain to determine the optimal user location.

This process in stage II can be represented as

$$\mathbf{w}_{(\mathcal{S}_{1},\mathcal{S}_{2},\mathcal{S}_{3})}^{\text{NF}} = \{ \mathbf{b}(\theta_{n}^{(\mathcal{S}_{1})}, \phi_{n}^{(\mathcal{S}_{2})}, r_{n}^{(\mathcal{S}_{3})}) \mid \mathcal{S}_{1} \in [0, \pi],$$

$$\mathcal{S}_{2} \in \left[-\frac{\pi}{2}, \frac{\pi}{2} \right], \mathcal{S}_{3} \in \mathcal{M} \}, \quad (11)$$

where $\mathcal{M} = \{r_{\min}, \dots, r_{\max}\} \in \mathbb{C}^{(1,S_3)}$, and S_3 is the number of samples in the distance domain. When the search distance exceeds the near-field range, the beam pattern degenerates into a far-field form without spatial focusing. In this case, the proposed joint angle-distance search strategy naturally reduces to a conventional angular-domain search, making it equally applicable to far-field users. Therefore, our algorithm samples $(S_3 - 1)$ points within the near-field range, and directly samples the last point at a longer far-field distance once the near-field range is exceeded. The $r_{
m max}$ represents the maximum radius distance in the near-field scenario, with each distance logarithmically sampled as:

$$r_i = r_{\min} \cdot \left(\frac{r_{\max}}{r_{\min}}\right)^{\frac{i-1}{S_3-1}}, \quad i = 1, 2, \dots, S_3.$$
 (12)

Based on the angular domain code book, we denote
$$(\hat{\theta}, \hat{\phi}) = \arg\max_{\theta, \phi} (|\mathbf{b}(\theta, \phi, r) \mathbf{w}_{(\mathcal{S}_1, \mathcal{S}_2)}^{\mathrm{FF}}|^2). \tag{13}$$

The optimal distance can be obtained based on near-field beam training as

$$\hat{r} = \arg \max_{r} (|\mathbf{b}(\theta, \phi, r) \mathbf{w}_{(\hat{\theta}, \hat{\phi}, \mathcal{S}_3)}^{\text{NF}}|^2). \tag{14}$$

B. 3D Two Stage Hierarchical Near-, Far-Field Beam Training

Due to the excessive number of samples required and the activation of all transmit elements during each sampling in the exhaustive beam training, significant training overhead is incurred, particularly in RHS architectures with a large number of transmission elements. To address this, a hierarchical beam training scheme is applied.

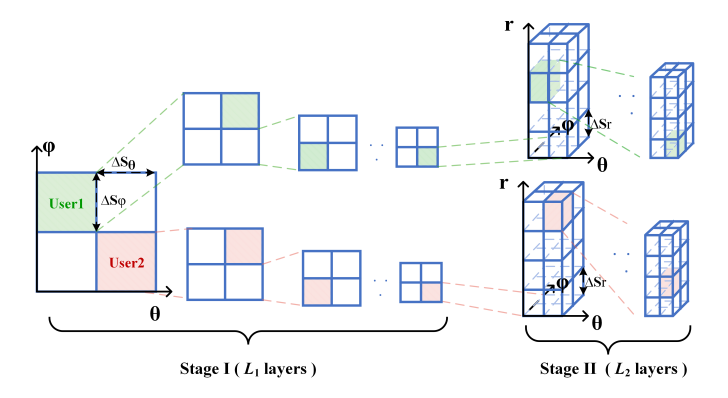


Illustration of the proposed two-stage hierarchical beam training Fig. 3. scheme.

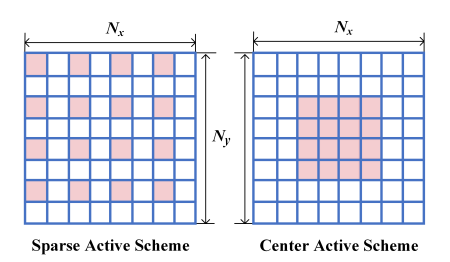


Fig. 4. Illustration of element activation locations in the proposed two-stage hierarchical beam training scheme.

The basic idea of hierarchical beam training is to initially search for a coarse user direction using wide beams and then progressively refine the user's spatial direction with narrower beams. The corresponding far-field hierarchical codebook can be implemented using either deactivation techniques or a combination of sub-array and deactivation techniques [24]. In this scheme, the union of the angle and distance domains covered by all codewords in each hierarchical layer should encompass the entire domain. Furthermore, the coverage region of any codeword in a given layer should be fully covered by the union of several codewords in the next layer. Additionally, within each layer, all codewords can be derived from a single codeword by beam rotation, ensuring uniform size and geometric shape.

The procedure of the proposed two-stage hierarchical beam training scheme is shown in Fig. 3. The total number of layers in our hierarchical codebook can be set as $L_t = L_1 + L_2 =$ $\log_2(N)$, with the upper- and lower-level codebooks consisting of L_1 and L_2 , respectively.

In the bottom layers L_1 , the optimal direction can be identified by hierarchically searching the angular regions in each layer. Based on the designed upper-level codebook, a quadtree-based beam search can be used to search both on the

angular and distance regions. In the first stage, $S_1^{(I)}$ and $S_2^{(I)}$ samples are taken in the azimuth and elevation domains, respectively, for each layer. In the *l*th layer, the codebook contains a total of $\left(S_1^{(I)}S_2^{(I)}\right)^l$ codewords, collected as $\mathcal{M}_l^{(I)}$. Assume that in the first stage, the $P_1 = \left(i_1^{(I)}, j_1^{(I)}\right)$ th codeword is sampled. In the subsequent lth layers, the coarse direction is then estimated as

$$\{\hat{\theta}_{l}, \hat{\phi}_{l}\} = \mathcal{M}_{l}^{(I)} \left\{ P_{l-1}(1) + \left(i_{l}^{(I)} - \frac{i_{l}^{(I)} + 1}{2} \right), \right.$$

$$\left. P_{l-1}(2) + \left(j_{l}^{(I)} - \frac{j_{l}^{(I)} + 1}{2} \right) \right\}. \quad (15)$$

In Stage II, based on the coarse direction estimated in Stage I, a near-field beam training process is applied to search across both angular directions and distance. For far-field users, where the channel response degenerates to a distance-invariant planar wavefront, the additional distance sampling has negligible impact on the beamforming performance, effectively reducing the process to a conventional angular search.

Suppose that $S_1^{(II)}$, $S_2^{(II)}$, and $S_3^{(II)}$ samples are taken in the azimuth, elevation, and distance domains, respectively, for each layer. In the lth layer, the codebook contains a total of $\left(S_1^{(II)}S_2^{(II)}S_3^{(II)}\right)^{(l-L_1)}$ codewords, collected as $\mathcal{M}_l^{(II)}$. Assume that in the (L_1+1) th layer, the $P_{L_1+1}=(i_{L_1+1}^{(II)},j_{L_1+1}^{(II)},z_{L_1+1}^{(II)})$ th codeword is sampled. In the subsequent the lth layers, the coarse direction is then estimated as

$$\{\hat{\theta}_{l}, \hat{\phi}_{l}, \hat{r}_{l}\} = \mathcal{M}_{l}^{(II)} \left\{ P_{l-1}(1) + \left(i_{l}^{(II)} - \frac{i_{l}^{(II)} + 1}{2} \right), \right.$$

$$P_{l-1}(2) + \left(j_{l}^{(II)} - \frac{j_{l}^{(II)} + 1}{2} \right),$$

$$P_{l-1}(3) + \left(z_{l}^{(II)} - \frac{z_{l}^{(II)} + 1}{2} \right) \right\}.$$

$$(16)$$

The beam gain of the codeword ${\bf w}$ along the position (θ,ϕ,r) is defined as

$$\mathcal{G}(\mathbf{w}, \theta, \phi, r) = |\mathbf{w}^H \mathbf{b}(\theta, \phi, r)|. \tag{17}$$

In the hierarchical beam training scheme, the number of active elements differs in each layer to generate beams of varying widths, allowing for a search from a wide range to a narrow range. In the practical case, the RHS elements are tightly arranged in a constrained area, and hence, the effect of mutual coupling should be carefully taken into consideration. To better study the effect of the distance between activated antennas on mutual coupling, we proposed two schemes, where the active location maps are shown in Fig. 4. In the following, we introduce the layout of the activation element of the two schemes, and the simulation results will be presented in section V.

The first is the center-active scheme, where an active index l_a is used to activate 2^{l_a} elements in the first layer, located in the center of the surface. The number of active elements doubles in each subsequent layer until all elements are fully activated.

The second scheme is a sparse active scheme, where $N_{a,l} = N/(L_1 - l_a - l)$ elements are activated in the lth layer. The sparse active matrix is defined as U, with the following dimensions

$$u_x = \lceil \sqrt{\frac{N_{a,l}N_x}{N_y}} \rceil, \quad u_y = \lceil \sqrt{\frac{N_{a,l}}{u_x}} \rceil.$$
 (18)

TABLE II
IMPERFECT HARDWARE FREQUENCY RESPONSE OF RHS ELEMENTS
UNDER DIFFERENT CONSTRAINTS.

Mode	Frequency response						
Amplitude-only	$\psi \in [a, b], b > a > 0$						
Binary Amplitude	$\psi \in d \cdot \{0, 1\}, d > 0$						
Lorentzian Phase Constrain	$\psi \in \left\{ \frac{j + e^{j\zeta}}{2} \right\}, \zeta \in [0, 2\pi]$						

To determine the number of active antennas in the horizontal and vertical directions, denoted as u_x and u_y , respectively, we compute u_x as $u_x = \left\lfloor \sqrt{\frac{N_{a,l} \cdot N_x}{N_y}} \right\rfloor$ and subsequently calculate u_y as $u_y = \left\lfloor \frac{N_{a,l}}{u_x} \right\rfloor$.

 u_y as $u_y = \left\lfloor \frac{N_{a,l}}{u_x} \right\rfloor$. The spacing between active antennas in the horizontal direction is given by $\Delta_x = \frac{N_x}{u_x+1}$, while the spacing in the vertical direction is defined as $\Delta_y = \frac{N_y}{u_y+1}$. The positions of the active antennas are then determined by placing them at indices x_i and y_j in the horizontal and vertical directions, respectively, where $x_i = \lfloor i \cdot \Delta_x \rfloor$ and $y_j = \lfloor j \cdot \Delta_y \rfloor$, for $i = 1, \dots, u_x$ and $j = 1, \dots, u_y$.

The resulting activation matrix U is an $N_x \times N_y$ matrix where the element U(x,y) is set to 1 if the antenna at position (x,y) is active and 0 otherwise. Mathematically, this can be expressed as

$$U(x,y) = \begin{cases} 1 & \text{if } x = x_i \text{ and } y = y_j, \\ 0 & \text{otherwise.} \end{cases}$$
 (19)

This method ensures that $N_{a,l}$ active antennas are distributed throughout the array with the horizontal and vertical maximum spacing possible. The training overhead of these two schemes is analyzed in Section IV.

C. Practical Beam Training Scheme

In this section, we present a joint codeword optimization algorithm aimed at maximizing the achievable rate at the receiving end. This is achieved by jointly optimizing the beamforming matrix at the transmission side and the phase shift matrix of the RHS, while accounting for the imperfect hardware frequency response of RHS elements under various constraints, as detailed in the Table II [13] [31].

The aim of designing a codeword is to make the beam pattern obtained by the codeword as close as possible to the ideal codeword \mathbf{w}^* . We can easily obtain the theoretical optimal codeword by SVD decomposition as in [10]. Upon obtaining the theoretical optimal codeword \mathbf{w}_k^* for each user, and defining $\mathbf{W}^* = [\mathbf{w}_1^*, \dots, \mathbf{w}_K^*]^T$, the practical codeword under a hybrid RHS architecture can be formulated as a minimization problem as

$$\min_{\psi, \mathbf{v}_k} \sum_{k}^{K} \|\mathbf{w}_k^* - \mathbf{F} \mathbf{\Phi} \mathbf{v}_k\|^2$$
s.t.
$$\mathbf{F} = \text{Diag}\{\psi_1, \psi_2, \dots, \psi_N\}.$$
(20)

Here, we propose a alternative optimization (AO) algorithm to optimize the holographic beamforming matrix \mathbf{F} and the active beamforming vector \mathbf{v}_k alternatively. When fixing the value of \mathbf{F} , the value of \mathbf{v}_k can be directly solved by the Least Squared (LS) method as

Algorithm 1 AO Optimization Algorithm for Hybrid Beamforming under Hardware Constraints

```
1: Initialize \psi randomly under constraints.
2: \mathbf{F} \leftarrow \mathrm{Diag}(\psi), \ \mathbf{v}_k \leftarrow \mathrm{pinv}(\mathbf{F}\mathbf{\Phi})\mathbf{w}_k^*
for i = 1 to max_iter do
   4: Update \mathbf{v_k} using (21).
   if Binary Amplitude Mode then
      5: Compute all binary combinations in each \psi_n satis-
      fying (22).
      if f_n(\psi_n) < f_n(\psi_{opt}) then
          6: \psi_{opt} = \psi_n.
   else
      7: Compute gradient \nabla f(\psi) using (24) or (27).
      8: Update \psi using the gradient descent algorithm and
      project constraints by (25) or (28).
   end if
   9: Update F.
end for
10: Return \mathbf{v}, \psi, \mathbf{F}, \mathbf{w}_k = \mathbf{F} \mathbf{\Phi} \mathbf{v}_k.
```

$$\mathbf{v}_{\text{opt },k} = \text{pinv}(\mathbf{F}\mathbf{\Phi})\mathbf{w}_k^*, \tag{21}$$

where the $pinv(\cdot)$ defines the pseudo-inverse of matrix. Then, for the given value of \mathbf{v}_k , the optimization problem of solving \mathbf{F} under different hardware constraints can be expressed as

$$\min_{\psi} \sum_{k}^{K} \|\mathbf{w}_{k}^{*} - \mathbf{F} \mathbf{\Phi} \mathbf{v}_{\text{opt },k}\|^{2}$$
s.t. $\psi_{n} \in \{\text{constraint in Table II}\}$

$$\mathbf{F} = \text{Diag}\{\psi_{1}, \psi_{2}, \dots, \psi_{N}\}.$$
(22)

The objective function can be written as

$$f(\psi) = \|\mathbf{W}^* - \mathbf{F}\mathbf{\Phi}\mathbf{V}\|^2,\tag{23}$$

where $\mathbf{V} = [\mathbf{v}_1, \dots, \mathbf{v}_K]$. To obtain the solution to (22) under the discrete binary amplitude constraint, we apply an exhaustive search, where all combinations of $\psi_1, \psi_2, \dots, \psi_N$, when $\psi_n \in d \cdot \{0, 1\}$ are tested to minimize the objective function. However, the computational complexity of the exhaustive search method is extremely high. In this case, we apply a highly efficient individual search method proposed in [14], where each ψ_n is determined separately in each iteration. This method naturally satisfies the convergence condition that the square error between the theoretical codeword and the practical codeword in each iteration decreases, which greatly reduces the computational complexity in the exhaustive search.

When solving (22) under the continuous constraints of the amplitude-only and Lorentzian phase constraints, we apply the gradient descent optimization method. Let us look at the gradient of the objective function for the two cases. For the amplitude-only constraints case, the gradient of the objective function (23) is given by

$$\nabla_{\psi} f(\psi) = -2\text{Re}\left[(\mathbf{\Phi} \mathbf{V}) \odot (\mathbf{W}^* - \text{Diag}(\psi)\mathbf{\Phi} \mathbf{V})\right], \quad (24)$$

and the update rule is

$$\psi^{(i+1)} = \psi^{(i)} - \alpha \nabla_{\psi} f(\psi^{(i)}), \ \psi^{(i+1)} \in [a, b], \ b > a > 0.$$
(25)

For the Lorentzian phase constraints case, as detailed in the Table II, we define the hardware constraint for the Lorentzian mode as

$$\psi \in \left\{ \frac{j + e^{j\zeta}}{2} \right\}, \quad \zeta \in [0, 2\pi]. \tag{26}$$

The gradient of the objective function (23) is expressed as

$$\begin{split} \nabla_{\zeta} f(\zeta) &= -2 \mathrm{Re} \Bigg[\Bigg(\mathbf{\Phi} \mathbf{V} \odot \Bigg(\mathbf{W}^* - \mathrm{Diag} \left(\frac{1}{2} (j + e^{j\zeta}) \right) \mathbf{\Phi} \mathbf{V} \Bigg) \Bigg) \\ & \odot \left(\frac{1}{2} j e^{j\zeta} \right) \Bigg], \quad (27) \end{split}$$

with the update rule is given by

$$\zeta^{(i+1)} = \zeta^{(i)} - \alpha \nabla_{\zeta} f(\zeta^{(i)}), \ \psi = \frac{1}{2} \left(j + e^{j\zeta} \right),$$
(28)

where $\zeta \in [0, 2\pi]$ represents the Lorentzian-type phase parameter governing the electromagnetic response of each RHS element, as defined in Table II. The proposed optimization process is detailed in Algorithm 1.

Having detailed the practical codeword design, we now analyze the fundamental beam properties of RHS-based architectures, with a particular focus on asymptotic orthogonality and training overhead in Section IV.

IV. ANALYSIS OF ASYMPTOTIC ORTHOGONALITY AND TRAINING OVERHEAD

To further analyze the impact of the RHS size and shape on the properties of near-field beam focusing vectors, this section investigates the asymptotic orthogonality of near-field beam focusing vectors for RHSs of different sizes. Additionally, this section examines the training overhead of the proposed beam training schemes in various 3D spatial configurations.

In contrast to existing works that consider beam orthogonality under idealized far-field assumptions, this section provides a near-field asymptotic analysis tailored to RHS structures with rectangular and square geometries. The impact of aperture shape on depth resolution and spatial focusing accuracy is theoretically and numerically characterized for the first time.

A. Asymptotic Orthogonality Analysis

In this section, we assume that there is only one user located in the Fresnel region and does not exceed the Rayleigh distance of the RHS transmitter. The distance between the (n_x, n_y) th element of the RHS and the user, based on the near-field spherical wave propagation model, can be expressed as in (29). The approximation (a) of (29) is derived using the second-order Taylor series expansion $\sqrt{1+x}=1+\frac{x}{2}-\frac{x^2}{8}+O(x^2)$. The approximation (b) of (29) has been shown in [15] to result in a beamforming loss of no more than 5% in the Fresnel region when the bilinear quadratic term is ignored. If the approximated near-field spherical wave model is adopted, the correlation of two beams $\mathbf{b}^H(r_l,\theta,\phi)$ and $\mathbf{b}^H(r_m,\theta,\phi)$

$$r^{(n_{x},n_{y})} = \sqrt{(r\cos\theta\sin\phi - \delta_{n_{x}}d)^{2} + (r\sin\theta\sin\phi - \delta_{n_{y}}d)^{2} + (r\cos\theta)^{2}}$$

$$\stackrel{(a)}{\approx} r - n_{x}d\cos\theta\sin\phi - n_{y}d\sin\theta\sin\phi + \frac{n_{x}^{2}d^{2}}{2r}\left(1 - \cos^{2}\theta\sin^{2}\phi\right) + \frac{n_{y}^{2}d^{2}}{2r}\left(1 - \sin^{2}\theta\sin^{2}\phi\right) - \frac{n_{x}n_{y}d^{2}\cos\theta\sin\theta\sin^{2}\phi}{r}$$

$$\stackrel{(b)}{\approx} r - n_{x}d\cos\theta\sin\phi - n_{y}d\sin\theta\sin\phi + \frac{n_{x}^{2}d^{2}}{2r}\left(1 - \cos^{2}\theta\sin^{2}\phi\right) + \frac{n_{y}^{2}d^{2}}{2r}\left(1 - \sin^{2}\theta\sin^{2}\phi\right).$$

$$|\mathbf{b}^{H}(r_{l}, \theta, \phi)\mathbf{b}(r_{m}, \theta, \phi)| = \left|\sum_{N_{x}}\sum_{N_{y}} e^{jk\left(n_{x}^{2}d^{2}\left(1 - \cos^{2}\theta\sin^{2}\phi\right) + n_{y}^{2}d^{2}\left(1 - \sin^{2}\theta\sin^{2}\phi\right)\right)\left(\frac{1}{2r_{l}} - \frac{1}{2r_{m}}\right)}\right|$$

$$\approx \left|\int_{-N_{x}/2}^{N_{x}/2} \int_{-N_{y}/2}^{N_{y}/2} e^{jk\left(n_{x}^{2}d^{2}\left(1 - \cos^{2}\theta\sin^{2}\phi\right) + n_{y}^{2}d^{2}\left(1 - \sin^{2}\theta\sin^{2}\phi\right)\right)\left(\frac{1}{2r_{l}} - \frac{1}{2r_{m}}\right)} dn_{x} dn_{y}\right| \stackrel{(c)}{\approx} |G(\beta_{1})G(\beta_{2})|.$$

$$(30)$$

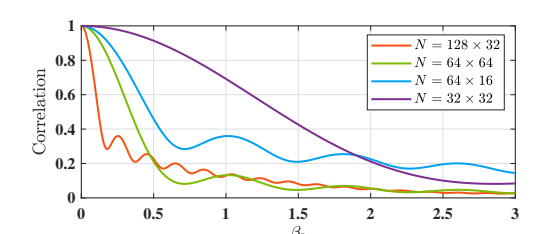


Fig. 5. Numerical results of the correlation as a function of β_0 for different RHSs shapes in a system operating at 30 GHz, sampled at $\theta=\pi/3$.

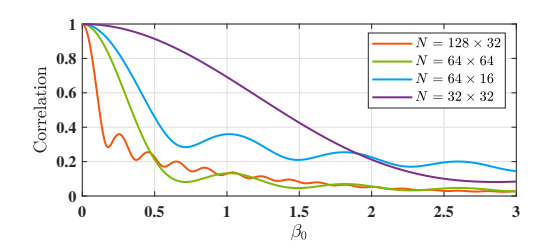


Fig. 6. Numerical results of the correlation as a function of β_0 for different RHSs shapes in a system operating at 30 GHz, sampled at $\theta \approx \pi/2$.

vectors focusing in the same direction but different distances can be formulated as (30). The approximation (c) of (29) has been proven in [15] where $G(\beta) = \frac{C(\beta) + jS(\beta)}{\beta}$, with $C(\cdot)$ and $S(\cdot)$ denoting the Fresnel functions written as $C(x) = \int_0^x \cos\left(\frac{\pi}{2}t^2\right) \mathrm{d}t$ and $S(x) = \int_0^x \sin\left(\frac{\pi}{2}t^2\right) \mathrm{d}t$. In (30), the parameter is derived as

$$\beta_1 = \sqrt{\frac{N_x^2 d^2 \left(1 - \cos^2 \theta \sin^2 \phi\right)}{2\lambda} \left| \frac{1}{r_l} - \frac{1}{r_m} \right|}, \tag{31}$$

$$\beta_2 = \sqrt{\frac{N_y^2 d^2 \left(1 - \sin^2 \theta \sin^2 \phi\right)}{2\lambda} \left|\frac{1}{r_l} - \frac{1}{r_m}\right|}.$$
 (32)

Let $\beta_0=\sqrt{\frac{d^2}{2\lambda}\left|\frac{1}{r_l}-\frac{1}{r_m}\right|}$, then the β_1 and β_2 can be expressed as

$$\beta_1 = \sqrt{N_x^2 \left(1 - \cos^2 \theta \sin^2 \phi\right)} \beta_0,\tag{33}$$

and

$$\beta_2 = \sqrt{N_x^2 \left(1 - \sin^2 \theta \sin^2 \phi\right)} \beta_0. \tag{34}$$

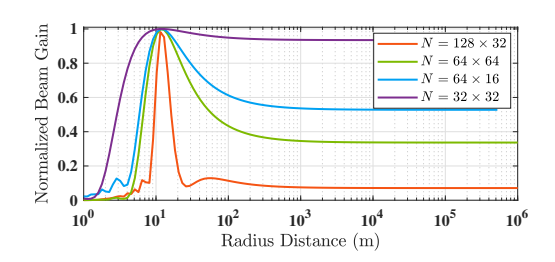


Fig. 7. Normalized beam gain under RHSs operating at 30 GHz with different size while focusing on the same point at $\theta = \pi/3$, $\phi = \pi/6$, and r = 15 m.

The numerical results for the correlation of beams as a function of β_0 at different distances but in the same direction are shown in Fig. 5 and Fig. 6 for various values of θ_l and different RHS sizes, with $\phi = \pi/6$.

From (29) and (30), we observe that the asymptotic correlation decay between beams focusing at different distances depends on the spatial aperture size along both dimensions. Given a fixed total number of elements, a rectangular RHS (with greater disparity between N_x and N_y) exhibits stronger beam decorrelation in the distance domain due to the enhanced variation of β_1 and β_2 . This implies improved depth resolution in near-field beam focusing. As shown in Fig. 5 and Fig. 6, the beam correlation as a function of β_0 decays more rapidly when the RHS surface is rectangular, indicating enhanced beam orthogonality in radial distance. This conclusion is further supported by the gain profile in Fig. 7, where a rectangular RHS exhibits a narrower 3 dB beam depth [32] and faster gain decay along the distance axis compared to a square RHS, thereby demonstrating higher distance resolution and supporting the assertion that rectangular surfaces offer superior beam orthogonality in the distance domain.

Then, we analyze the correlation between the beams of $\mathbf{b}^H(r,\theta_l,\phi_l)$ and $\mathbf{b}^H(r,\theta_m,\phi_m)$ in the same direction but at a different distance, which can be expressed in (35), where $\epsilon_1 = \cos\theta_m \sin\phi_m - \cos\theta_l \sin\phi_l$, $\epsilon_2 = \sin\theta_m \sin\phi_m - \sin\theta_l \sin\phi_l$, $\epsilon_3 = \cos^2\theta_m \sin^2\phi_m - \cos^2\theta_l \sin^2\phi_l$ and $\epsilon_4 = \sin^2\theta_m \sin^2\phi_m - \sin^2\theta_l \sin^2\phi_l$.

In (35), the bilinear quadratic term involving ϵ_3 and ϵ_4 is coupled with the squared terms of the two angular parameters. In our two-stage hierarchical beam sweeping design,

$$\mathbf{b}^{H}(r,\theta_{l},\phi_{l})\,\mathbf{b}(r,\theta_{m},\phi_{m}) = \sum_{n_{x}}^{N_{x}} \sum_{n_{y}}^{N_{y}} e^{jk\left(\frac{n_{x}^{2}d^{2}}{2r}\epsilon_{3} + \frac{n_{y}^{2}d^{2}}{2r}\epsilon_{4}\right)} \times \sum_{n_{x}}^{N_{x}} \sum_{n_{y}}^{N_{y}} e^{jk(n_{x}d\epsilon_{1} + n_{y}d\epsilon_{2})}$$

$$= \sum_{n_{x}}^{N_{x}} e^{jk\left(\frac{n_{x}^{2}d^{2}}{2r}\epsilon_{3} + n_{x}d\epsilon_{1}\right)} \times \sum_{n_{y}}^{N_{y}} e^{jk\left(\frac{n_{y}^{2}d^{2}}{2r}\epsilon_{4} + n_{y}d\epsilon_{2}\right)} = \int_{-N_{x}/2}^{N_{x}/2} e^{j\frac{2\pi}{\lambda}\left(n_{x}d\epsilon_{1} + n_{x}^{2}d^{2}\frac{\epsilon_{3}}{2r}\right)} dn_{x} \int_{-N_{y}/2}^{N_{y}/2} e^{j\frac{2\pi}{\lambda}\left(n_{y}d\epsilon_{2} + n_{y}^{2}d^{2}\frac{\epsilon_{4}}{2r}\right)} dn_{y}.$$
(35)

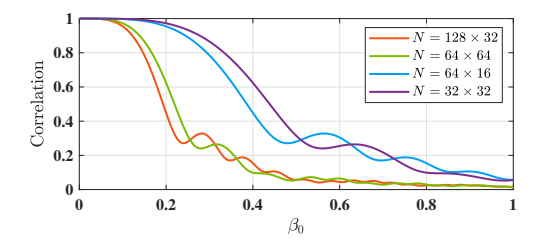


Fig. 8. Numerical results of the correlation as a function of β_0 for different RHSs shapes in a system operating at 30 GHz, sampled at $\theta_l = \pi/3$.

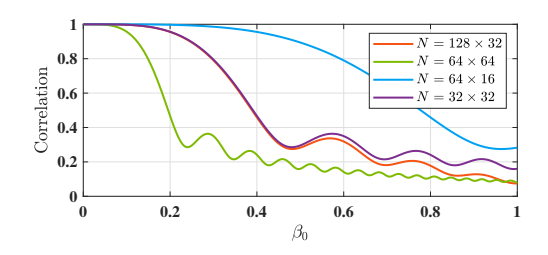


Fig. 9. Numerical results of the correlation as a function of β_0 for different RHSs shapes in a system operating at 30 GHz, sampled at $\theta_l \approx \pi/2$.

the primary direction is identified through far-field beam search. Therefore, we consider the correlation between two far-field beams oriented in different directions. To simplify the equation, we approximate it to a far-field scenario by assuming $\frac{1}{r} \approx 0$, then (35) can be simplified as

$$\int_{-N_x/2}^{N_x/2} e^{j\frac{2\pi}{\lambda}n_x da\beta_0} dn_x \int_{-N_x/2}^{N_y/2} e^{j\frac{2\pi}{\lambda}n_y db\beta_0} dn_y,$$
 (36)

where

$$a = \frac{\epsilon_1}{\sqrt{\frac{d^2}{2\lambda}\left(\epsilon_1^2 + \epsilon_2^2\right)}}, \quad b = \frac{\epsilon_2}{\sqrt{\frac{d^2}{2\lambda}\left(\epsilon_1^2 + \epsilon_2^2\right)}}.$$
 (37)

By defining

$$\beta_1 = \frac{da\beta_0}{4\lambda} N_x, \quad \beta_2 = \frac{db\beta_0}{4\lambda} N_y, \tag{38}$$

we can transform the integrals in (36) into the form of Fresnel functions as

$$\int_0^{\beta_1} \frac{e^{j\frac{\pi}{2}t_1^2}}{\beta_1} dt_1 \int_0^{\beta_2} \frac{e^{j\frac{\pi}{2}t_2^2}}{\beta_2} dt_2 = |G(\beta_1)G(\beta_2)|.$$
 (39)

The numerical results for the correlation of beams as a function of β_0 at different distances but in the same direction are shown in Fig. 8 and Fig. 9 for various values of θ_l and different RHS sizes, with $\phi_m = \phi_l = \pi/6$ and $\theta_m = \pi/3$.

As observed from Fig. 8 and Fig. 9, the convergence speed of the beam correlation with respect to β_0 varies across different angles for RHSs of different shapes at the two sampled angles. This indicates that, when the distance is fixed but the angle varies, the impact of the RHS shape on beam correlation is not constant. Specifically, the rectangular and square RHSs can provide different correlations for beam focus at different angles. Therefore, in this analysis scenario, the shape of the RHS is not considered a primary factor.

In summary, based on the analysis of RHS beam characteristics in different directions and distances, choosing a rectangular RHS surface for transmission is advantageous for precise beam depth control in near-field scenarios. Consequently, in subsequent simulations, we mainly adopt a rectangular antenna array design. However, it is important to note that the beam control accuracy and beamwidth in each direction are also influenced by the number of elements along that direction. Therefore, the number of elements on the edges of the antenna array must be carefully chosen.

B. Training Overhead Analysis

In this section, we analyze and compare the training overhead of three beam training schemes: the two-stage centering active (CA) hierarchical beam training scheme, the two-stage sparse active (SA) hierarchical beam training scheme, and the two-stage exhaustive search scheme. The training overhead is defined as the total number of operations required to activate and search across the antenna elements during the beam training process.

For the CA scheme, the number of activated antennas in the first layer is given by $N/2^{l_a}$, where N is the total number of antennas, and l_a is the starter index, which controls the number of active antennas in the initial layer. In subsequent layers, the number of activated antennas doubles until all N antennas are fully activated in the final layer. The total training overhead T_{CA} is calculated as

$$T_{\text{CA}} = \sum_{l=1}^{L_1} S_1^{(I)} S_2^{(I)} \cdot \min \left\{ \frac{N}{2^{l_a + l - 1}}, N \right\} + L_2 \cdot S_1^{(II)} S_2^{(II)} S_3^{(II)} N, \quad (40)$$

where L_1 and L_2 represent the number of layers in the first and second stages, respectively. $S_1^{(I)}$ and $S_2^{(I)}$ denote the number of samples in the angular domain in the first stage, while $S_1^{(II)}$, $S_2^{(II)}$, and $S_3^{(II)}$ represent the number of samples in the angular and distance domains in the second stage, respectively.

In the SA scheme, the number of activated antennas starts with N/l_a in the first layer and gradually increases by a factor

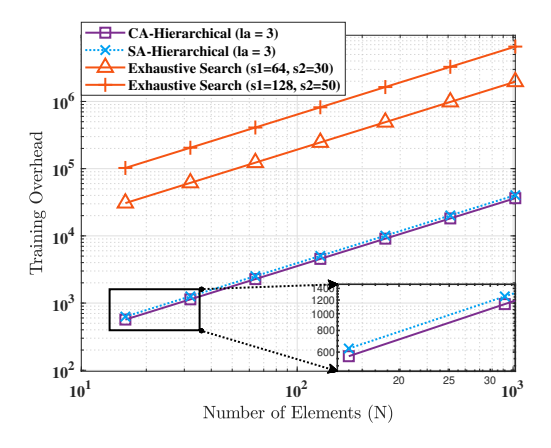


Fig. 10. Training overhead of various beam training schemes (CA: Center Active, SA: Sparse Active) for different numbers of RHS elements.

of l-1 in each subsequent layer until all antennas are activated. The total training overhead $T_{\rm SA}$ is expressed as

$$T_{SA} = \sum_{l=1}^{L_1} S_1^{(I)} S_2^{(I)} \cdot \min \left\{ \frac{N}{L_1 - l_a - l + 1}, N \right\} + L_2 \cdot S_1^{(II)} S_2^{(II)} S_3^{(II)} N.$$
 (41)

The Exhaustive Search scheme involves activating all N antennas in all layers. After determining the direction in the angular domain, a distance domain sampling is performed. The training overhead $T_{\rm EX}$ for this scheme is given by

$$T_{\text{EX}} = (S_1 S_2 + S_3) \cdot N, \tag{42}$$

where S_1 and S_2 are the sampling numbers in the two angles of the angular domain and S_3 is the sampling number in the distance domain. Figure 10 illustrates the training overhead as a function of the number of antennas N for the three beam training schemes while $S_1^{(I)} = S_2^{(I)} = S_1^{(II)} = S_2^{(II)} = 2$ and $S_3^{(II)} = 4$. The results show that the CA and SA schemes significantly reduce the training overhead compared to the exhaustive search scheme, particularly as the number of antennas increases. Although the CA scheme has slightly lower training overhead than the SA scheme, the simulation performance of these schemes is presented in Section V.

C. Computational Complexity Analysis

In the following, we quantify the computational complexity of the proposed AO-based beam training algorithm. In each iteration, let K be the number of users, M denotes the number of RF chains, and N represents the number of RHS elements. The primary computational steps include a pseudoinverse operation of size $N \times M$ with complexity $\mathcal{O}(NM)$, and a gradient computation per element of ψ or ζ , incurring a per-user cost of $\mathcal{O}(N)$. Therefore, for K users, the total complexity per iteration scales approximately as $\mathcal{O}(KNM)$.

Then, in each iteration, the total complexity is approximately

$$\mathcal{O}(K(NM+N)) = \mathcal{O}(KNM). \tag{43}$$

In practical settings for example using $N=512,\,M=16,\,K=4,$ this leads to a per-iteration complexity on the

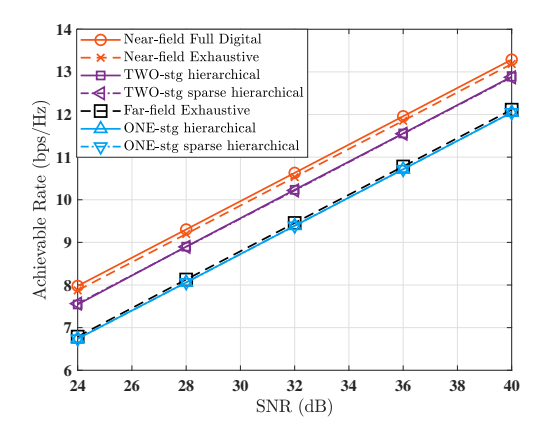


Fig. 11. Comparison of the achievable rate in MISO system, when varying the beam training scheme .

order of 3×10^4 operations. Given the rapid convergence within fewer than 8 iterations (as shown in Fig. 13), the total computational complexity remains under 2.4×10^5 operations. This is substantially lower than that of the exhaustive search, which requires $\mathcal{O}(N \cdot S_1 S_2 S_3) \approx 10^7$ beam evaluations per user, for example, when $S_1 = S_2 = 64$ and $S_3 = 50$.

Compared to fully digital architectures, which assume perfect per-element control and incur full-size matrix SVD with complexity $\mathcal{O}(N^3)$, our scheme offers substantial savings in both computation and control signaling, making it well suited for real-time multi-user scenarios with dynamic channel conditions.

V. SIMULATION RESULTS

In this section, we present the simulation results of the achievable rate to validate the effectiveness of our proposed beam training schemes under the proposed hybrid RHS structure, considering different modes of RHS surface hardware constraints. The Monte Carlo method is used with 10^5 iterations. Specifically, we consider an RHS-aided MIMO communication system with $N_x=32,\ N_y=16,\ f=30$ GHz, $M=32,\ {\rm and}\ \beta=\left(\frac{\lambda}{4\pi}\right)^2=-53$ dB. The reference SNR of the system is defined as SNR = $\frac{P\beta N}{r^2\sigma^2}$ [16], where the noise power is set to $\sigma^2=-70$ dBm. Moreover, the achievable rate is given by

$$R = \sum_{k=1}^{K} \log_2 \left(1 + \frac{\Gamma_k P \beta N |\mathbf{h}_k^H(\theta_k, \phi_k, r_k) \mathbf{w}_k|^2}{r_k^2 \sigma^2} \right), \quad (44)$$

where Γ_k is a power allocation parameter which can be calculated based on the water-filling method [42].

In Fig. 11, we compare the achievable rate versus SNR for different beam training schemes under both near-field and far-field conditions. The size of the RHS elements is set to $d_x = d_y = \lambda/2$, and the user is randomly positioned within the angular search domain and the near-field distance domain. We observe that the proposed two-stage exhaustive beam training scheme performs nearly as well as the perfect CSI based fully digital result. Additionally, the two proposed hierarchical schemes achieve satisfactory performance with

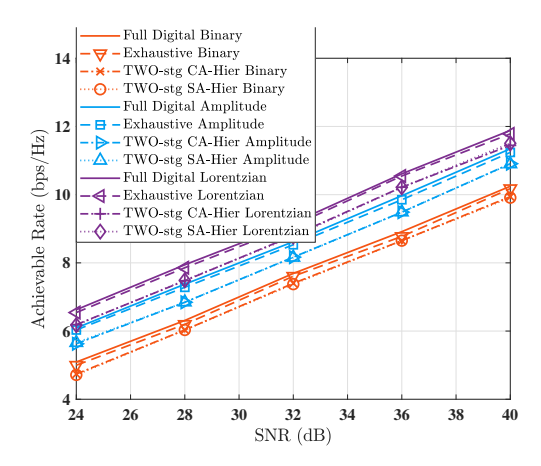


Fig. 12. Comparison of the achievable rate in MISO system, when varying the beam training scheme of exhausted and hierarchical under different hardware constrains (binary, amplitude and Lorenzian constrain).

lower training overhead, without significantly compromising the rate performance compared to the exhaustive near-field beam training scheme. It is also evident that our proposed scheme consistently outperforms the far-field exhaustive and hierarchical beam training scheme.

In Fig. 12, we simulate the performance of different beam training schemes under various RHS hardware constraints, as detailed in Table II with a = 0, b = 1, and d = 1. From the simulation results, we observe that the practical beam training scheme achieves satisfactory performance compared to the fully digital design with hardware constraints. The Lorentzian phase constrain based scheme outperforms the amplitude-only constrained and binary amplitude constrained based schemes by providing a continuous frequency response in both the real and imaginary parts. Additionally, the amplitude-only constrained scheme performs better than the binary amplitude constrained scheme due to its continuous frequency response, as opposed to the binary response. Furthermore, the CA and SA hierarchical schemes exhibit similar performance, despite differing training overhead. For brevity, we refer to the center active and sparse active hierarchical beam training schemes as CA and SA, respectively. Since these two schemes activate a different number and arrangement of RHS elements in each layer, mutual coupling effects also warrant consideration, where the corresponding performance is shown in Fig. 16.

Fig. 11 and Fig. 12 demonstrated that the CA and SA hierarchical schemes exhibit similar performance. Hence, we only employ the CA scheme with lower overhead training in Fig. 13 and Fig. 14 as an example of the hierarchical beam training scheme to analyze other influencing factors. In Fig. 13, we simulate the performance of different beam training schemes under various hardware constraints of RHS with respect to the number of iterations in the proposed alternating optimization algorithm, as detailed in Algorithm 1. Although the proposed AO algorithm does not offer strict theoretical convergence guarantees, each iteration involves either a closed-form update via pseudo-inverse or a gradient descent step that monotonically decreases the cost function. The results show that the convergence speed of our proposed alternating

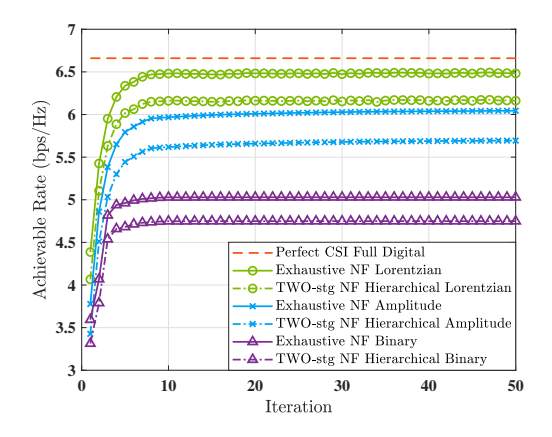


Fig. 13. Comparison of the achievable rate when varying the iteration times in alternative optimization optimization.

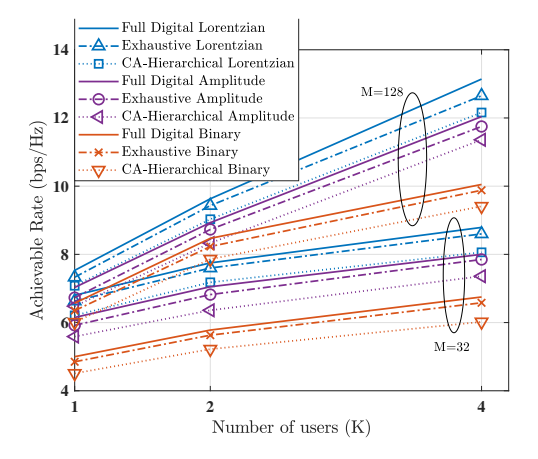


Fig. 14. Comparison of the achievable rate when varying the number of users and the number of feeds under different beam training scheme of exhausted and hierarchical under different hardware constrains (binary, amplitude and Lorenzian constrain).

optimization algorithm is excellent. Furthermore, the algorithm converges within fewer than 8 iterations, validating its practical efficiency and stability in the RHS-aided hybrid beamforming architecture.

In Fig. 14, we simulate the performance of different beam training schemes in a multi-user scenario with various RHS hardware constraints and different numbers of feeds in an RHS-aided hybrid beamforming architecture. The results show that the system's performance increases almost linearly with the number of users when the number of feeds is M=128. However, when M=32, the system cannot provide a very high rate for multi-user scenarios when the number of users exceeds four. Additionally, it can be seen that the continuous Lorentzian phase constrain mode and the amplitude-only constrained mode achieve better performance than the binary-constrained scheme as the number of users increases, due to their continuously adjustable amplitude and phase characteristics.

In practice, CSI estimation for RHS systems is highly challenging due to the large number of elements. To evaluate robustness against imperfect CSI, we model the estimated channel as $\hat{h}_k^H = h_k^H + h_{k,e}^H$. The channel estimation er-

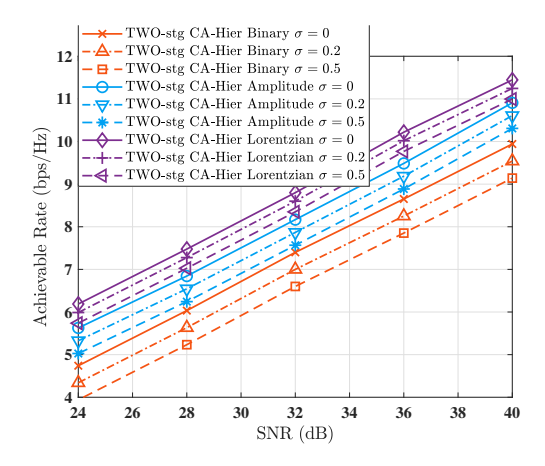


Fig. 15. Comparison of the achievable rate when varying the varying the channel estimation error under different hardware constrains (binary, amplitude and Lorenzian constrain).

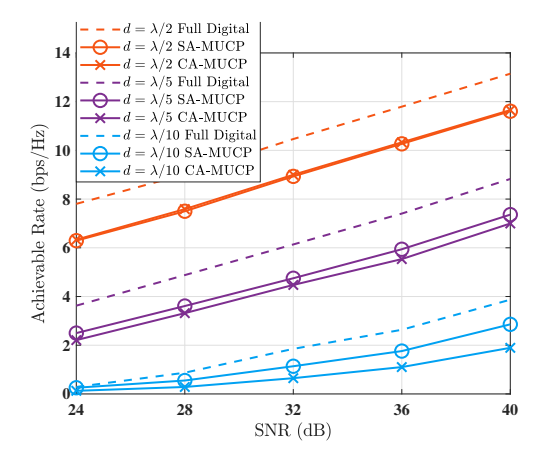


Fig. 16. Comparison of the achievable rate when varying RHS element size and hierarchical beam training scheme when existing mutual coupling between RHS elements.

ror components $h_{k,e}^H$ follow a complex normal distribution $\mathcal{CN}(0,\sigma I)$, where σ denotes the variance of the estimation error [40] [43]. In Fig. 15, we evaluate the impact of imperfect CSI under different hardware constraint models. The CSI perturbation is modeled as complex Gaussian noise with zero mean and standard deviation σ . As σ increases from 0 to 0.5, the achievable rate of all schemes declines, with the binary model showing the most degradation due to its coarse quantization characteristics. In contrast, the Lorentzian-based design exhibits superior robustness, maintaining higher performance across all SNR levels and CSI error variances. These results clearly demonstrate the effectiveness and robustness of the proposed beam training scheme.

As the previous simulation results show, the CA and SA hierarchical schemes exhibit similar performance, despite differing training overhead. However, we take the mutual coupling between the RHS elements into consideration because the active elements' locations of the RHS differ between the CA and SA schemes.

For the general case where there exists mutual coupling, we adopt the Z-parameter representation, which is a standard way to model this effect. The $\mathbf{C} \in \mathbb{C}^{N \times N}$ is the mutual coupling

matrix given by [13]

$$\mathbf{C} = (Z_{\mathbf{A}} + Z_{\mathbf{L}}) \left(\mathbf{Z} + Z_{\mathbf{L}} \mathbf{I} \right)^{-1}, \tag{45}$$

where $Z_{\rm A}$ is the antenna impedance and $Z_{\rm L}$ is the load impedance. Both $Z_{\rm A}$ and $Z_{\rm L}$ are fixed to 50 Ohms . The mutual impedance matrix ${\bf Z}$ is formulated as

$$\mathbf{Z} = \begin{pmatrix} Z_{A} & Z_{12} & \dots & Z_{1N} \\ Z_{21} & Z_{A} & \dots & Z_{2N} \\ \vdots & \vdots & \dots & \vdots \\ Z_{N1} & Z_{N2} & \dots & Z_{A} \end{pmatrix}.$$
(46)

The off-diagonal elements of the mutual impedance matrix **Z** when $m \neq n$ are calculated as:

$$Z_{mn} = 60 \operatorname{Ci}(\kappa d_{mn}) - 30 \operatorname{Ci}(\kappa \sqrt{d_{mn}^2 + \iota^2 + \iota}) - 30 \operatorname{Ci}(\kappa \sqrt{d_{mn}^2 + \iota^2 - \iota}) - 60j \operatorname{Si}(\kappa d_{mn}) + 30j \operatorname{Si}(\kappa \sqrt{d_{mn}^2 + \iota^2 + \iota}) + 30j \operatorname{Si}(\kappa \sqrt{d_{mn}^2 + \iota^2 - \iota})$$
(47)

where $\kappa=\frac{2\pi}{\lambda}$ denotes the wavenumber and d_{mn} represents the distance between dipoles m and n. The symbol ι is used to denote the length of the dipoles, we define $\iota=10/\lambda$ here. The functions $\mathrm{Ci}(x)$ and $\mathrm{Si}(x)$ refer to the cosine integral function and the sine integral function, respectively. In addition, j represents the imaginary unit. The sine integral function $\mathrm{Si}(x)$ is defined as:

$$\operatorname{Si}(x) = \int_0^x \frac{\sin(t)}{t} \, dt,\tag{48}$$

while the cosine integral function Ci(x) is defined as

$$\operatorname{Ci}(x) = -\int_{x}^{\infty} \frac{\cos(t)}{t} dt. \tag{49}$$

In Fig. 16, we simulate the performance of different beam training schemes versus various reference SNRs with different RHS element sizes. The results shown in the figure correspond to a scenario where the total number of active elements equals N/8. We observe that, when considering the effects of mutual coupling, the SA hierarchical scheme achieves better performance than the CA scheme due to the sparser distribution of active elements on the surface. Moreover, the system provides a higher achievable rate as the size of the RHS elements increases.

VI. CONCLUSION

In this paper, we proposed a novel hierarchical beam training scheme for RHS-aided MIMO systems, which enables efficient 3D beam scanning in near-field and far-field scenarios. Our proposed scheme is also suited to addressing the challenges of RHS design, including hardware constraints and mutual coupling effects. The introduction of practical beam training and activation schemes further enhances the feasibility of RHS-based systems. The findings on beam orthogonality in different RHS shapes provide valuable insight to optimize beamforming performance, which makes it better suited for complex MIMO environments.

The proposed hierarchical beam training framework is inherently suitable for 3D space applications, enabling potential extensions to UAV-assisted communications as well as integrated sensing and communications. Future work may explore joint beam training and localization strategies to support 3D user sensing and tracking.

REFERENCES

- W. Tang et al. Path loss modeling and measurements for reconfigurable intelligent surfaces in the millimeter-wave frequency band. *IEEE Trans. Commun.*, 70(9):6259–6276, September 2022.
- [2] Y. Zeng and R. Zhang. Millimeter wave MIMO with lens antenna array: A new path division multiplexing paradigm. *IEEE Trans. Commun.*, 64(4):1557–1571, April 2016.
- [3] S. Zeng et al. Reconfigurable intelligent surfaces in 6G: Reflective, transmissive, or both? *IEEE Commun. Lett.*, 25(6):2063–2067, June 2021.
- [4] A. Pizzo, T. L. Marzetta, and L. Sanguinetti. Spatially-stationary model for holographic MIMO small-scale fading. *IEEE J. Sel. Areas Commun.*, 38(9):1964–1979, September 2020.
- [5] R. Deng, Y. Zhang, H. Zhang, B. Di, H. Zhang, and L. Song. Reconfigurable holographic surface: A new paradigm to implement holographic radio. *IEEE Veh. Technol. Mag.*, 18(1):20–28, March 2023.
- [6] S. Zeng, H. Zhang, B. Di, H. Qin, X. Su, and L. Song. Reconfigurable refractive surfaces: An energy-efficient way to holographic MIMO. *IEEE Commun. Lett.*, 26(10):2490–2494, October 2022.
- [7] M. Cui, Z. Wu, Y. Lu, X. Wei, and L. Dai. Near-field MIMO communications for 6G: Fundamentals, challenges, potentials, and future directions. *IEEE Commun. Mag.*, 61(1):40–46, January 2023.
- [8] R. Deng, B. Di, H. Zhang, Y. Tan, and L. Song. Reconfigurable holographic surface: Holographic beamforming for metasurface-aided wireless communications. *IEEE Trans. Veh. Technol.*, 70(6):6255–6259, June 2021.
- [9] R. Deng, B. Di, H. Zhang, Y. Tan, and L. Song. Reconfigurable holographic surface-enabled multi-user wireless communications: Amplitude-controlled holographic beamforming. *IEEE Trans. Wireless Commun.*, 21(8):6003–6017, August 2022.
- [10] Q. Li, M. El-Hajjar, Y. Sun, I. Hemadeh, A. Shojaeifard, and L. Hanzo. Energy-efficient reconfigurable holographic surfaces operating in the presence of realistic hardware impairments. *IEEE Trans. Commun.*, pages 1–1, 2024.
- [11] Q. Li, M. El-Hajjar, Y. Sun, and L. Hanzo. Performance analysis of reconfigurable holographic surfaces in the near-field scenario of cell-free networks under hardware impairments. *IEEE Trans. Wireless Commun.*, 23(9):11972–11984, 2024.
- [12] H. Zhang, N. Shlezinger, F. Guidi, D. Dardari, M. F. Imani, and Y. C. Eldar. Beam focusing for near-field multiuser MIMO communications. IEEE Trans. Wireless Commun., 21(9):7476–7490, September 2022.
- [13] J. Xu, L. You, G. C. Alexandropoulos, X. Yi, W. Wang, and X. Gao. Near-field wideband extremely large-scale MIMO transmissions with holographic metasurface-based antenna arrays. *IEEE Trans. Wireless Commun.*, pages 1–1, 2024.
- [14] Y. Lu, Z. Zhang, and L. Dai. Hierarchical beam training for extremely large-scale MIMO: From far-field to near-field. *IEEE Trans. Commun.*, 72(4):2247–2259, 2024.
- [15] Z. Wu and L. Dai. Multiple access for near-field communications: SDMA or LDMA? *IEEE J. Sel. Areas Commun.*, 41(6):1918–1935, 2023.
- [16] Y. Zhang, X. Wu, and C. You. Fast near-field beam training for extremely large-scale array. *IEEE Wireless Commun. Lett.*, 11(12):2625–2629, December 2022.
- [17] C. Wu, C. You, Y. Liu, L. Chen, and S. Shi. Two-stage hierarchical beam training for near-field communications. *IEEE Trans. Veh. Technol.*, 73(2):2032–2044, February 2024.
- [18] X. Wu, C. You, J. Li, and Y. Zhang. Near-field beam training: Joint angle and range estimation with DFT codebook. *IEEE Trans. Wireless Commun.*, pages 1–1, 2024.
- [19] J. Chen, F. Gao, M. Jian, and W. Yuan. Hierarchical codebook design for near-field mmwave MIMO communications systems. *IEEE Wireless Commun. Lett.*, 12(11):1926–1930, November 2023.
- [20] S. Zhang, B. Di, A. Kaushik, and Y. C. Eldar. Holographic-pattern based multi-user beam training in RHS-aided hybrid near-field and farfield communications. arXiv preprint arXiv:2411.04382, 2024.

- [21] Z. Wu, M. Cui, and L. Dai. Enabling more users to benefit from near-field communications: From linear to circular array. *IEEE Trans. Wireless Commun.*, 23(4):3735–3748, April 2024.
- [22] M. Cui and L. Dai. Channel estimation for extremely large-scale MIMO: Far-field or near-field? *IEEE Trans. Commun.*, 70(4):2663–2677, April 2022.
- [23] C. Zhou, C. Wu, C. You, and S. Shi. Near-field beam training with sparse DFT codebook. arXiv:2406.04262, June 2024. Available: http://arxiv.org/abs/2406.04262.
- [24] X. Shi, J. Wang, Z. Sun, and J. Song. Spatial-chirp codebook-based hierarchical beam training for extremely large-scale massive MIMO. *IEEE Trans. Wireless Commun.*, 23(4):2824–2838, April 2024.
- [25] S. Liu, X. Yu, Z. Gao, and D. W. K. Ng. Dpss-based codebook design for near-field xl-MIMO channel estimation. arXiv:2310.18180, October 2023. Available: http://arxiv.org/abs/2310.18180.
- [26] H. Jiang, Z. Wang, and Y. Liu. Sense-then-train: A novel beam training design for near-field MIMO systems. arXiv:2402.15634, February 2024. Available: http://arxiv.org/abs/2402.15634.
- [27] K. Zhi, C. Pan, H. Ren, K. K. Chai, C.-X. Wang, R. Schober, and X. You. Performance analysis and low-complexity design for XL-MIMO with near-field spatial non-stationarities. *IEEE J. Sel. Areas Commun.*, 42(6):1656–1672, 2024.
- [28] Q. Wu, G. Chen, Q. Peng, W. Chen, Y. Yuan, Z. Cheng, J. Dou, Z. Zhao, and P. Li. Intelligent reflecting surfaces for wireless networks: Deployment architectures, key solutions, and field trials. *IEEE Wireless Commun.*, pages 1–9, 2025.
- [29] T. Wu, C. Pan, K. Zhi, H. Ren, M. Elkashlan, J. Wang, and C. Yuen. Employing high-dimensional RIS information for RIS-aided localization systems. *IEEE Commun. Lett.*, 28(9):2046–2050, 2024.
- [30] T. Wu, C. Pan, K. Zhi, H. Ren, M. Elkashlan, C.-X. Wang, R. Schober, and X. You. Exploit high-dimensional RIS information to localization: What is the impact of faulty element? *IEEE J. Sel. Areas Commun.*, 42(10):2803–2819, 2024.
- [31] T. Sleasman, M. F. Imani, W. Xu, J. Hunt, T. Driscoll, M. S. Reynolds, and D. R. Smith. Waveguide-fed tunable metamaterial element for dynamic apertures. *IEEE Antennas Wireless Propag. Lett.*, 15:606–609, 2016.
- [32] E. Björnson, Ö. T. Demir, and L. Sanguinetti. A primer on near-field beamforming for arrays and reconfigurable intelligent surfaces. In 2021 55th Asilomar Conference on Signals, Systems, and Computers, pages 105–112, 2021
- [33] T. Wu, K. Zhi, J. Yao, X. Lai, J. Zheng, H. Niu, M. Elkashlan, K.-K. Wong, C.-B. Chae, and Z. Ding. Fluid antenna systems enabling 6G: Principles, applications, and research directions. arXiv preprint arXiv:2412.03839, 2024.
- [34] S. Yang, J. Yao, J. Tang, T. Wu, M. Elkashlan, C. Yuen, M. Debbah, H. Shin, and M. Valenti. Towards intelligent antenna positioning: Leveraging DRL for FAS-aided ISAC systems. *IEEE Internet Things* J., pages 1–1, 2025.
- [35] J. Zheng, X. Lai, T. Wu, M. Elkashlan, D. B. da Costa, C. Yuen, and F. Adachi. Unlocking FAS-RIS security analysis with block-correlation model. *IEEE Wireless Commun. Lett.*, 14(7):2029–2033, 2025.
- [36] S. S. A. Yuan, X. Chen, C. Huang, and W. E. I. Sha. Effects of mutual coupling on degree of freedom and antenna efficiency in holographic MIMO communications. *IEEE Open J. Antennas Propag.*, 4:237–244, 2023.
- [37] W. Liu, C. Pan, H. Ren, F. Shu, S. Jin, and J. Wang. Low-overhead beam training scheme for extremely large-scale ris in near field. *IEEE Trans. Commun.*, 71(8):4924–4940, August 2023.
- [38] Y. Liu, Z. Wang, J. Xu, C. Ouyang, X. Mu, and R. Schober. Near-field communications: A tutorial review. *IEEE Open J. Commun. Soc.*, 4:1999–2049, 2023.
- [39] K. Zhi, T. Yang, S. Li, Y. Song, T. Wu, and G. Caire. Holographic mimo multi-cell communications. arXiv preprint arXiv:2502.16669, 2025.
- [40] Y. Dong, Q. Li, S. X. Ng, and M. El-Hajjar. Reconfigurable intelligent surface relying on low-complexity joint sector non-diagonal structure. *IEEE Open J. Veh. Technol.*, 5:1106–1123, 2024.
- [41] M. Cui, L. Dai, Z. Wang, S. Zhou, and N. Ge. Near-field rainbow: Wideband beam training for XL-MIMO. *IEEE Trans. Wireless Commun.*, 22(6):3899–3912, 2023.
- [42] A. Goldsmith. Wireless Communications. Cambridge University Press, Cambridge, 2005.
- [43] L. Zou, Z. Pan, A. A. Alameer, H. Dahrouj, and M. El-Hajjar. Joint beamforming and combining design for mmwave integrated access and backhaul networks. *IEEE Open J. Commun. Soc.*, 5:503–513, 2024.



Yinuo Dong received the B.Eng. degree in Electronic Information Engineering from Changzhou University, Changzhou, China, in 2021, and the M.Sc. degree in Mobile Communications and Smart Networking from the University of Southampton, Southampton, U.K., in 2022. She is currently pursuing the Ph.D. degree with the Next Generation Wireless Communications Group, School of Electronics and Computer Science, University of Southampton. Her research interests include reconfigurable intelligent surfaces, near-field communications, holo-

graphic MIMO, and signal processing for advanced wireless systems.



Qingchao Li (Member, IEEE) received the B.Eng. degree from the University of Science and Technology Beijing, Beijing, China, in 2017, the M.S. degree from the University of Science and Technology of China, Heifei, China, in 2020, and the Ph.D. degree in wireless communications from the University of Southampton, Southampton, U.K., in 2024 under the University of Southampton-Interdigital Communications Inc. Fully Funded Scholarship. His research interests include reconfigurable intelligent surfaces, holographic MIMO and non-terrestrial

wireless networks. He was the recipient of 2022 Chinese Government Award for Outstanding Self-Financed Student Abroad and 2023 Doctoral College Research Award, University of Southampton.



Soon Xin Ng (S'99-M'03-SM'08) received the B.Eng. degree (First class) in electronic engineering and the Ph.D. degree in telecommunications from the University of Southampton, U.K., in 1999 and 2002, respectively. He is currently a Professor of Next Generation Communications at the University of Southampton. His research interests include adaptive coded modulation, coded modulation, channel coding, space-time coding, joint source and channel coding, iterative detection, OFDM, MIMO, cooperative communications, distributed coding, quantum

communications, quantum error correction codes, joint wireless-and-optical-fibre communications, game theory, artificial intelligence and machine learning. He has published over 300 papers and co-authored two John Wiley/IEEE Press books in this field.



Mohammed El-Hajjar (M'02, SM'14) is a Professor of Signal Processing for Wireless Communications in the School of Electronics and Computer Science in the University of Southampton. He is the recipient of several academic awards and has published a Wiley-IEEE book and more than 150 IEEE journal and conference papers and in excess of 10 patents. Mohammed's research interests include the design of intelligent and energy-efficient transceivers, MIMOs, millimeter wave communications, non-terrestrial networks and machine learning

for wireless communications. Mohammed's research is funded by the Engineering and Physical Sciences Research Council, the Royal Academy of Engineering and many industrial partners.